Surface plasmon lasers

Tenner, V.T.

Chapter 4

Measurement of the phase and intensity profile of surface plasmon laser emission

We study the near and far field radiation patterns of surface plasmon (SP) lasers in metal hole arrays and observe radially polarized vortex-vector laser beams in both near and far field. Besides the intensity profile, also the complementary phase profile is obtained with a beam block experiment, where we block part of the beam in the near field, measure the resulting changes in the far field, and retrieve the phase using an iterative algorithm. This phase profile provides valuable information on the feedback mechanisms and coherence of the laser and shows that our SP laser operates in a phase-slip mode instead of a pure dark mode. To explain our observations, we extend the standard model for distributed feedback (DFB) lasers by introducing a position dependence in the optical gain and refractive index.

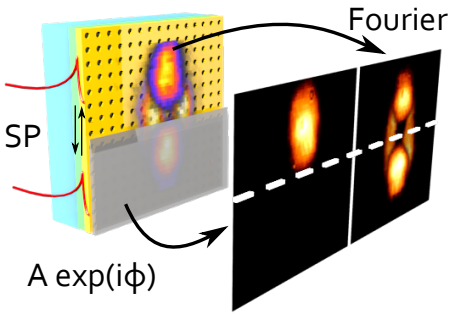

This chapter was previously published as:
V. T. Tenner, M. J. A. de Dood, and M. P. van Exter, *Measurement of the Phase and Intensity Profile of Surface Plasmon Laser Emission*, ACS Photonics **3**, 942 (2016)

4.1 Introduction

Optically coherent laser radiation can be generated if both gain and optical feedback are present in a medium. Our physical understanding of these phenomena originates from comparisons between measured intensity distributions and models of both the amplitude and the phase of the radiation. The optical phase is typically discarded because it evolves too fast to resolve directly with an optical detector or a camera. The inability to measure both amplitude and phase of the emitted laser radiation presents a recurring challenge in optics and limits progress in the field.

More ingenious schemes are needed to observe the phase using slow detectors. One of the simplest schemes uses the mixing of the amplitude and phase information of the light field upon propagation. At the laser exit the amplitude contains information where the light is emitted, while the phase profile contains information about the propagation direction. Recording the intensity distribution on different positions allows retrieval of the phase information by an iterative algorithm [66–68].

The ability to resolve both amplitude and phase is particularly relevant for lasers that emit non-standard beam profiles that are not yet fully understood. Examples of such lasers are surface-emitting distributed feedback lasers, such as photonic and plasmonic crystal lasers. Two-dimensional surface-emitting photonic-crystal-lasers often emit donut beams with azimuthal polarization [69], while surface plasmon lasers create radially polarized vector-vortex beams [20]. Devices can be tailored to emit other beam shapes [70], but information about the phase- and amplitude profile is scarce and has either low resolution [71] or an electrical contact blocks the view [72].

A better understanding of gain and feedback in plasmonic systems is important for improving photonics applications that use the strong confinement and light-matter interaction provided by plasmons. These applications include ultra sensitive molecule sensors (SERS) [3], anti-counterfeiting measures [73], perfect absorbers [74], ultra-fast optical modulators [75], as well as future metal-dielectric metamaterials consisting of arrays of plasmonic sub-wavelength elements [5, 6]. The strong plasmonic response of passive media is accompanied by Ohmic loss due to scattering of the free electrons in the material. Adding media with active gain can resolve this issue [19, 76, 77] and over-compensation typically leads to laser action, as has been demonstrated in two-dimensional metal particle arrays [28], and metal hole arrays [20].

In this chapter, we present the first experimental observation of the phase- and amplitude profile of a two-dimensional surface plasmon laser retrieved via the combination of a beam-block experiment and an iterative algorithm. The metal hole array in our study acts as a second order Bragg grating, which provides a natural output channel and enables easy observation of the intracavity field. Our observations go beyond the standard description of distributed feedback lasers. We extend the standard approach by including a position dependent gain and

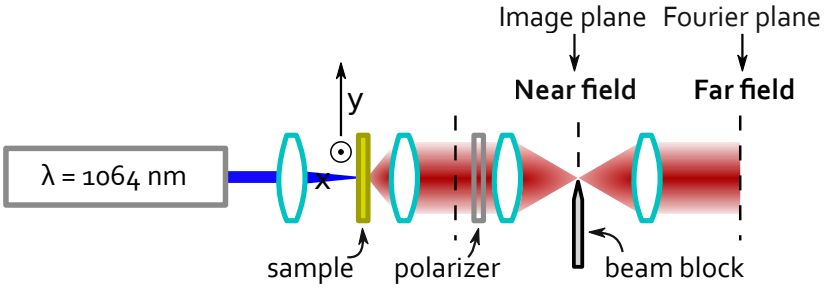

Figure 4.1: Schematic of the experimental setup to measure the amplitude and phase profile of the laser emission.

refractive index, which are both induced by the optical pump beam, and obtain good agreement between experiment and theory.

4.2 Device

The semiconductor-gold samples that we study contain metal hole arrays with a square lattice, with hole diameters of 160 nm and a lattice spacing of 470 nm (see Fig. 4.2a for a SEM image). The device dimensions studied here are 50x50 and 100x100 μm. The Au film is 100 nm thick and is deposited on a 127 nm $In_xGa_{1-x}As$ ($x = 0.536$) gain layer on an InP substrate (see Fig. 4.2e for a schematic side cut). Between the gold and the InGaAs, a thin InP spacer layer and a SiN passivation layer were incorporated. The gain layer is sufficiently thin such that the only supported optical mode is the surface plasmon (SP) mode. Similar samples are described in more detail in ref [20].

4.3 Experiment

Our experimental geometry is as shown in Fig. 4.1. The sample is mounted in a cryostat with optical access on both sides and cooled down to 80 K. We pump the active layer of the sample using a continuous wave laser with a wavelength of 1064 nm through the transparent InP substrate. The pump beam has a Gaussian profile that can be varied in size between 20 and 50 μm full width at half maximum. The light emitted by the SP laser is collected in transmission on the metal side of the device with a 20x microscope objective (NA = 0.4) combined with a tube lens (f = 200 mm) to create a 4-f imaging system. Hence, the optical field in the image plane is a scaled version of the radiative field at the sample; in this thesis, we call this the near field.

In some of the experiments we position a razor blade in the near field to block part of the beam. To inspect the near field, we image it with a lens (f = 100 mm) on a CCD camera. Subsequently, this lens is replaced by a lens with a longer focal distance (f = 200 mm) such that the far field is retrieved in the back-focal plane. A

bandpass filter ($\lambda = 1490 \pm 6$ nm) that transmits the laser light is used to reduce the broadband spontaneous emission in the measurements.

4.4 Results

Figure 4.2 show the measured near field (top) and far field (bottom) of the SP laser. Images are shown for the unpolarized light (b,f), with a linear polarizer transmitting y-polarized light (c,g) and with half of the near field blocked (d,h). The near field is donut shaped, i.e. it is circular with a dark center. The laser area is comparable to the size of the pump, being 40 μm in this case. The dark central spot is remarkable and raises questions about the apparent lack of energy in the center of the device. Figure 4.2c shows a polarization resolved measurement. Since this image rotates along when rotating the polarized axis, we conclude that the near field donut is radially polarized. The observation of a clear donut in the near field is only apparent when the pump beam is small enough. In our experiments, we observe that larger pump beams (up to 100 μm) result in a larger laser areas and spatial inhomogeneity. Nonetheless, there is always a dark spot somewhere, as expected for a topological defect. Under some experimental conditions the laser hops between several spatial modes with different locations of the dark spot, and hence the central dark spot becomes less visible after averaging.

Figures 4.2f-h show the observed far field intensity profiles and display that the far field is also a radially polarized donut beam. This similarity is not trivial and warrants further investigation. In order to observe the associated phase profile, we perform an experiment in which we block half of the near field with a razor blade and observe the far field. The resulting near field, shown in Fig. 4.2d, is trivial and presented mainly for didactic reasons. The resulting far field, shown in Figure 4.2h, depicts that the two lobed far field is now reduced to a single lobe, while the angle of the maximum emission is hardly changed. This observation provides valuable information about the phase profile of the near field, because it indicates the existence of a phase gradient in the near field.

To quantify the full two-dimensional phase profile of the optical field, we retrieve the phase profile with an iterative Gerchberg-Saxton-based algorithm [66], see Methods. We find that the retrieved near field phase exhibits a π-phase jump in the dark center of the device and exhibits a phase gradient in the radial direction, with a slope that increases towards the edge of the device. A cross section of this phase profile is depicted in Fig. 4.3c,g. These figures also show cross sections of the near and far field intensity profiles presented earlier in Fig. 4.2. The far field of the full beam has no light in the center, whereas there is emission along the surface normal in the beam block experiments. Because the far field of the full beam should be equal to the coherent sum of the two halves, the dark center in the far field must be formed by interference of emission from the two halves of the sample. This in turn indicates the existence of long range coherence across the sample. In the rest of this chapter we will discuss the implications of our observations and compare

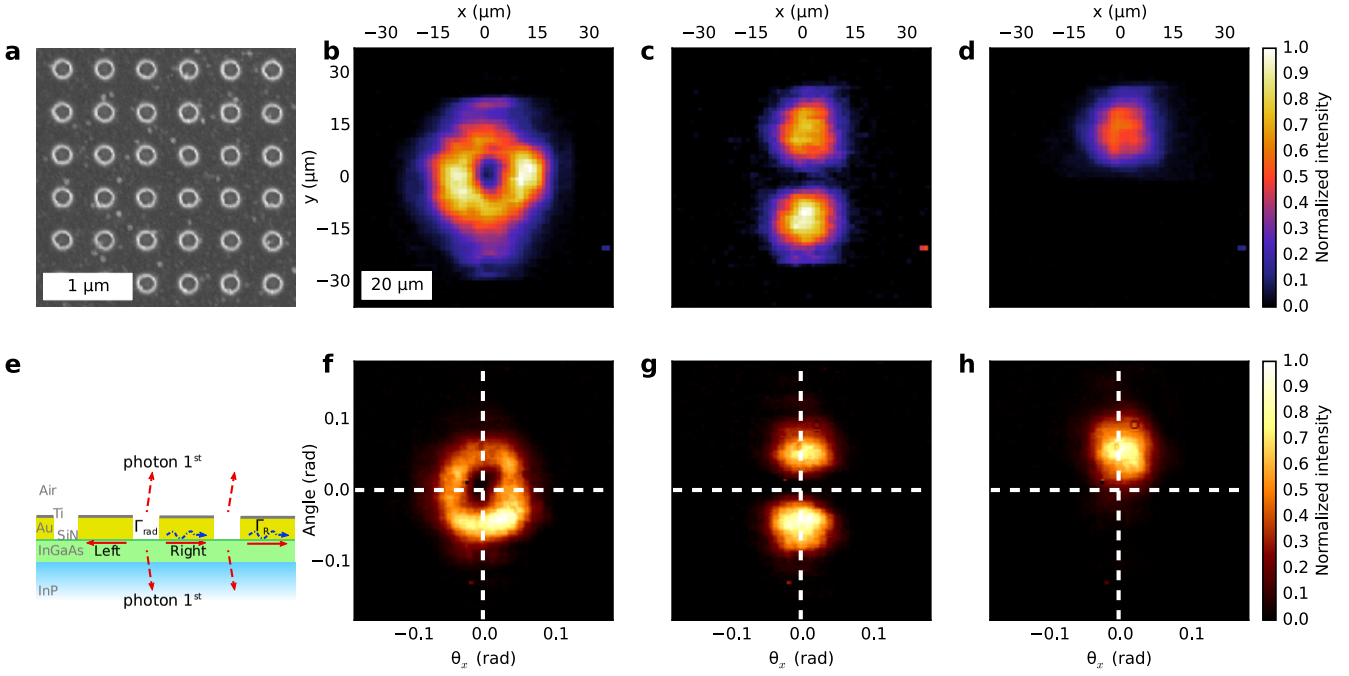

Figure 4.2: Our SP-laser and its emission, measured in near and far field. (a) Scanning electron microscopy image of the metal hole array. (e) Cross section through the sample, indicating the layer-stack, the left and right traveling waves and the emitted light. (b-d) Near field and (f-h) far field intensity profiles of a surface plasmon laser. (b,f) Show the donut shaped beams in both near and far field. (c,g) Show profiles observed behind a polarizer that transmits vertically polarized light. (d,h) Show what happens when we block the lower part of the near field. Vertical cross sections are shown in Fig. 4.3(c,g).

them with theory.

4.5 Discussion

We first compare our results with the standard DFB theory [35] for one dimensional systems with a finite size. In this theory, the field in the device is decomposed in two traveling waves, which are coupled by scattering at the holes. The relevant parameters are the length L of the device and the coupling rate κ. The product κL determines the behavior of the laser. This theory yields the threshold condition of the laser: wavelength, gain and the field profiles of the traveling waves.

The solutions are either symmetric or anti-symmetric around the center of the device. In an infinitely large index coupled system these are dark (non-radiating) and bright (radiating) modes, which are located at the exact center of the Brillouin-zone ($k = 0$) [37, 51, 78]. However, in a "real" laser, the coherence length ℓ_{coh} is limited by the finite sample size and the scattering [35], which breaks the description of a continuous band structure into discrete modes with a detuning from the Bragg wavelength. The relevant modes are at $\Delta k = \pi/\ell_{coh}$ and there is no mode at the center of the Brillouin-zone.

Scattering in the out-of-plane direction induces radiative loss, which increases the threshold of the radiative solution [79]. Our device operates in a transverse-magnetic (TM) mode and hence the coupled mode with the symmetric out-of-plane E-field distribution is the non-radiating mode with the lowest threshold, as explained in Appendix 4.A.

Figure 4.3a,b displays the calculated symmetric coupled mode solution of the standard DFB theory for our measured backscatter rate $\kappa/\beta_0 = 0.012$ [37], device length $L = 50\,\mu\text{m}$, and refractive index $n_0 = 3.268$ [52], corresponding to $\kappa L = 8$. The calculated near field shown in Fig. 4.3a contains the essential features of Fig. 4.3c: it has two lobes with opposite sign, indicated by a π-phase-jump in center of the device. However, in contrast to the experiment the calculated phase in each of the lobes is almost constant. As a consequence, the far field profiles depicted in Fig. 4.3e are very different from the observations depicted in Fig. 4.3g: the calculated profile is too narrow and is oscillatory at larger angles. Furthermore, the emission by half of the device is incorrectly predicted to be a single lobe located close to the surface normal.

To explain our observations we extend the standard DFB theory by introducing a position dependence of the gain and refractive index (see Appendix 4.A for derivation). Both are mainly set by the carrier density, which is position dependent due to inhomogeneous pumping and diffusion, and to a lesser extent by the local temperature associated with heating of the device. We model the local gain and index as the Gaussian profile of the pump beam, and note that deviations from an exact Gaussian shape are unimportant. In the center of the pumped area there is an effective gain, as discussed below, while outside the pumped area there is an effective loss (negative gain), which is mainly caused by absorption in the gain

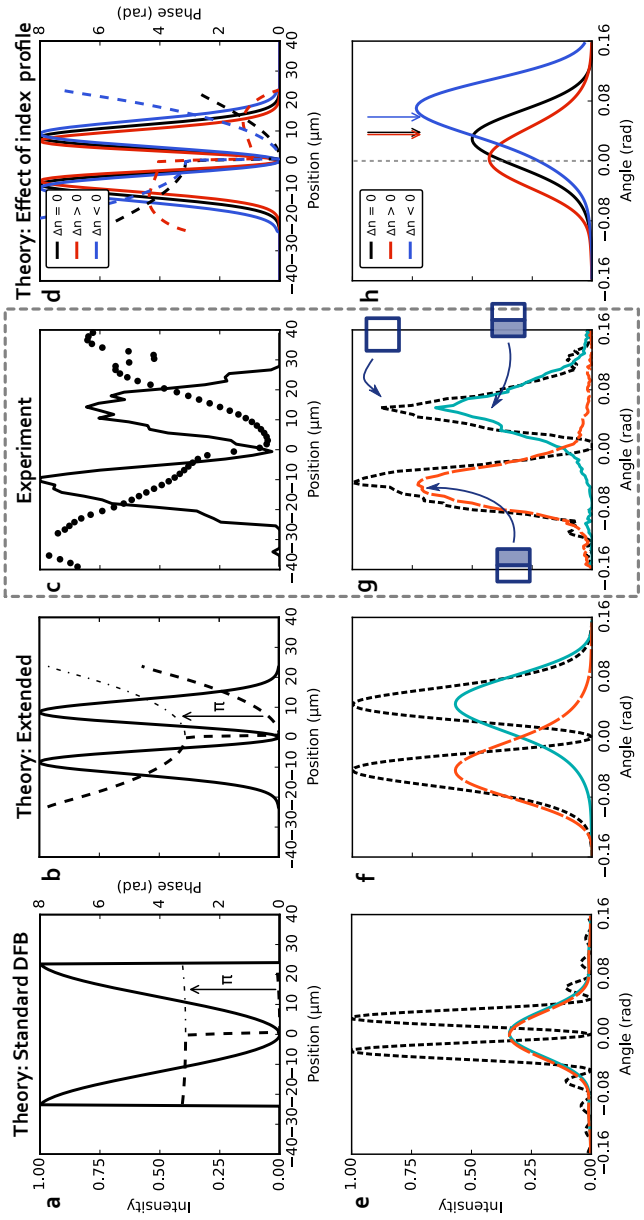

Figure 4.3: Cross sections through the center along the vertical direction of the (a-d) near field and (e-h) far field. In (a-d), the solid lines show the intensity envelope and the dashed lines show the phase of the near field. To stress the symmetry in (a,b), a π-shifted copy of the phase is displayed as a dashed-dotted line. In (e-h), the dashed curves show the far field intensity profiles of the full beam, while the colored curves show the resulting far fields when blocking the right (red dashed) or left (blue solid) half of the near field. The framed figures (c,g) are the experimental data taken from Fig. 4.2 and the reconstructed phase of the near field. The other figures are based on theory: (a,d) Standard DFB theory with uniform gain and index, (b,f) extended theory that includes a position dependent gain and refractive index, (d,h) extended theory with variations in the magnitude of the index profile. Note that (h) only displays the far field for one blocking condition. The arrows indicate the opening angle of the beam without beam block.

layer. We solve the coupled mode equations by an active mirror approach [63], which is relatively simple and powerful, as explained in Appendix 4.A. The resulting fields at the threshold are shown in Fig. 4.3b,f. The phase in the near field now increases towards the edge of the samples, very comparable to our measurements. Hence, also the far field profiles of the beam block experiment are very similar to our observations: the maxima are now at the same angle as the lobes of the full beam.

Figure 4.3d,h illustrates the predicted effect of index guiding and anti-guiding on the laser, with a Gaussian gain and index profile, with $\Delta n = 0$, $\Delta n = +0.13$, and $\Delta n = -0.13$ between the pumped center and the unpumped edges. The differences are best visible in a beam block experiment (see Fig. 4.3h), where the angle of the maxima of the lobe moves inwards for $\Delta n > 0$ and outwards for $\Delta n < 0$. The near fields depicted in Fig. 4.3d show index guiding for $\Delta n > 0$, and index anti-guiding for $\Delta n < 0$. This guiding can also be interpreted as a plasmonic bandgap with spatial dependence [80, 81]. Our experimental data can be best fitted with $\Delta n = -0.05$, which is consistent with the typical refractive index changes of pumped bulk material [82].

The gain profile, in contrast to the index profile, leads to guiding, because the effective gain in the center of the pumped area is higher than its surroundings. The gain and loss used in the model have realistic values: The unpumped areas have an effective intensity loss of [52] $\approx 3000\,\mathrm{cm}^{-1}$. At the threshold, the net gain in the center is $\approx 340\,\mathrm{cm}^{-1}$. The required material intensity gain is the sum of the net gain and the Ohmic loss of our device with transparent InP [52] ($270\,\mathrm{cm}^{-1}$), divided by the confinement factor in the gain layer [19] (0.32) and it is around $2000\,\mathrm{cm}^{-1}$, which is a reasonable number for a semiconductor operated at high carrier densities [38, 83].

For completeness we note that we have used a one-dimensional model to describe a two- (or even three)-dimensional system. Hence the derived numbers may differ somewhat from reality. From literature on DFB theory in two dimensions [84, 85], we expect that the influence of such 2D coupling on the derived numbers is rather low in our system, because it already operates in the overcoupled regime and the 2D coupling is small compared to the 1D coupling. In earlier work [37, 52] we measured $k_2/k_3 \approx 0.3$, where k_2 and $k_3 = \kappa$ are the scattering rates of respectively 90° and 180° scattering [84]. This extra coupling will only marginally change the detuning [85] and threshold [84]. Other authors have extended the standard DFB theory to two dimensions to answer the question under which conditions the symmetric mode can lase [86]. These analyses confirm that 2D DFB lasers are expected to emit donut shaped beams.

4.6 Conclusion

This chapter reports the first measurement and reconstruction of the phase and the amplitude of surface plasmon laser emission. Our two-dimensional plasmonic-

crystal emits donut-shaped and radially-polarized light, both in the near field and in the far field. By blocking half of the laser emission we retrieve the phase of the emission and demonstrate the existence of long range coherence and lasing in a symmetric non-radiative mode. Our observations cannot be explained with the standard DFB theory, which assumes a device with uniform properties. We extend this theory by introducing position dependence of the gain and refractive index and find good agreement with our measurements on surface-emitting DFB lasers. This provides the following three insights: First, due to the round trip phase condition, the laser is in a phase-slip mode and not in a dark mode and hence the laser can radiate. Second, we attribute the lack of emission in the center of the near field interference between in-plane counter-propagating waves. Third, the central zero in the far field also results from the symmetry of the lasing mode and demonstrates the existence of long range coherence over the full sample.

Our results demonstrate a powerful method to analyze surface-emiting lasers. This method can also be deployed on surface plasmon lasers with other lattice symmetries or on photonic-crystal lasers in order to understand and improve their characteristics. Furthermore, our results indicate that much of the current knowledge about one- and two-dimensional photonic-crystal lasers can be applied to understand and improve surface plasmon lasers.

4.7 Methods

The phase of the fields is retrieved with an iterative Gerchberg-Saxton-based algorithm [66–68]. The near and far field measurements are used as support for the algorithm. The phase is retrieved for 3 sets of conjugate measurements in parallel: (i) the full polarization resolved measurements shown in Fig. 4.2c,g and measurements with either a blocked (ii) bottom (Fig. 4.2d,h) or (iii) top (measurements not shown). Every 5th iteration, the reconstructed phase of alternately the bottom or top part is applied on the full near field reconstruction. After 30 iterations, we end with 10 iterations on the full fields. The algorithm convergences and is stable to noise.

Acknowledgement

The authors thank Dirk E. Boonzajer Flaes for his discussions about the iterative algorithm, Matthias Saba for his discussions about surface plasmon lasers, and Peter J van Veldhoven and Erik Jan Geluk for their help in fabricating the samples at the COBRA Research Institute of the Technische Universiteit Eindhoven, The Netherlands. This work is part of the research program of the Foundation for Fundamental Research on Matter (FOM), which is part of the Netherlands Organization for Scientific Research (NWO).

Appendices

4.A Distributed feedback theory with a position dependence of the gain and refractive index

In this supplement, we derive a coupled mode theory that extends the standard DFB theory with a position dependence of the gain and refractive index. We explain how the equations can be solved both in the time domain and the spatial domain and compare them with previous efforts. We solve the equations with an active mirror approach and demonstrate that this method is very flexible and fast.

The temporal and spatial evolution of the optical field in a one-dimensional distributed feedback (DFB) structure can be derived from the optical wave equation by using the slowly-varying approximation. This derivation can be found in many text books [35, 82] and only the main results for a device with a second-order Bragg grating and TM polarized mode are stated here. We express the optical field as the sum of a rightward R and leftward S traveling wave and write each of them as a slowly-varying envelope multiplied by a reference wave [35]:

$$E(x;t) = [R(x,t)\,e^{i\beta_0 x} + S(x,t)\,e^{-i\beta_0 x}]e^{-i\omega_0 t}, \tag{4.A.1}$$

where ω_0 is the reference frequency. The reference wave vector $\beta_0 \equiv 2\pi/\Lambda = n_0\omega_0/c$ is fixed by the lattice spacing Λ, and is linked to the reference frequency via the reference index n_0. The dielectric constant is expanded in Fourier components and the resulting terms are sorted. The resulting dimensionless coupled-mode equation that describe the temporal and spatial evolution of the envelope functions R and S is:

$$\frac{1}{\omega_0}\frac{\partial}{\partial t}R + \frac{1}{\beta_0}\frac{\partial}{\partial x}R = \left(i\frac{\Delta n(x) - i\alpha(x)}{n_0} - \frac{\kappa_{\text{out}}}{\beta_0}\right)R + \left(\frac{i\kappa_{\text{back}} + \kappa_{\text{out}}}{\beta_0}\right)S \tag{4.A.2}$$

$$\frac{1}{\omega_0}\frac{\partial}{\partial t}S - \frac{1}{\beta_0}\frac{\partial}{\partial x}S = \left(i\frac{\Delta n(x) - i\alpha(x)}{n_0} - \frac{\kappa_{\text{out}}}{\beta_0}\right)S + \left(\frac{i\kappa_{\text{back}} + \kappa_{\text{out}}}{\beta_0}\right)R \tag{4.A.3}$$

The slow changes in the complex index $\hat{n} = n_0 + \Delta n(x) + i\alpha(x)$ are parameterized by the dimensionless gain $\alpha(x)$ and refractive index difference $\Delta n(x)$, which both have a gradual position dependence. The gain is related to the material intensity gain $g\,[\text{cm}^{-1}]$ via $\alpha(x) = g(x)n_0\Lambda/4\pi$. Fast changes in the complex index are governed by higher-order Fourier components, as discussed below. Dispersive effects are neglected ($\omega\frac{\partial n}{\partial \omega} \ll n$). The two counter propagating waves are coupled by scattering at the periodic corrugations with backscatter coupling parameter κ_{back}. This scattering also induces dissipative out of plane coupling κ_{out}.

The coupling κ_{back} and κ_{out} are related to Fourier components of the corrugation [82, 84, 87]. For a 2nd order DFB, the backscatter is relatively simple and is given by the second order ($2\beta_0$) Fourier component. The output coupling is related to

the first (β_0) component in a more complicated way; it induces radiative loss of the energy of the R and S modes and κ_{out} depends approximately on the square of the first Fourier component.

The radiative loss and coupling induced by the out-of-plane scattering is most easily understood in the standing wave basis with the symmetric $R+S$ mode and the anti-symmetric $R-S$ mode. For a transverse-magnetic (TM) polarized mode, R and S denote the out-of-plane component of the E-field. The emission from the device depends on the in-plane fields, which are out-of-phase with the out-of-plane E-field[37]. Hence, the symmetric $R+S$ mode is a dark mode without loss, with anti-nodes in the out-of-plane E-field at the holes, while the anti-symmetric $R-S$ mode is radiative and experiences double radiative losses [37, 79, 84, 87]. This is mathematically described by the four coupling terms κ_{out} in Eqs. (4.A.2) and (4.A.3).

There are two different approaches to solve Eqs. (4.A.2)-(4.A.3): either in the time domain or in the space domain. In chapters 2, 3, and 5 we considered the *time dynamics of the Bloch modes of an infinitely large system* and labeled these modes by the angle θ at which they emit to free space, i.e. we set $\frac{\partial}{\partial x}R = k_0\theta R$ and $\frac{\partial}{\partial x}S = k_0\theta S$, where $k_0 = \omega_0/c$ is the wave vector in air. This yields the bandstructure of the crystal [37, 52] and was used to determine the dimensionless coupling rates $\kappa_{\text{back}}/\beta_0 = \gamma/\omega_0$ and $\kappa_{\text{out}}/\beta_0 = \Gamma_{rad}/\omega_0$.

Equations (4.A.2)-(4.A.3) can also be solved in the spatial domain, by looking for *the stationary eigenmodes of a finite-size system* at the laser threshold, i.e. the modes that vary in time as $\exp(-i\omega t)$, where $\omega \equiv \omega_0 + \delta\omega$ such that $\frac{\partial}{\partial t}R = -i\delta\omega R$ and $\frac{\partial}{\partial t}S = -i\delta\omega S$. The change of the fields over one unit cell can now be described by:

$$\Lambda\frac{\partial}{\partial x}\begin{pmatrix} R \\ S \end{pmatrix} = 2\pi\Bigg[(i\frac{\delta\omega}{\omega_0} + i\frac{\Delta n(x) - i\alpha(x)}{n_0})\begin{pmatrix} 1 & 0 \\ 0 & -1 \end{pmatrix} \\ -i\frac{\kappa_{\text{back}}}{\beta_0}\begin{pmatrix} 0 & 1 \\ -1 & 0 \end{pmatrix} - \frac{\kappa_{\text{out}}}{\beta_0}\begin{pmatrix} 1 & -1 \\ 1 & -1 \end{pmatrix}\Bigg]\begin{pmatrix} R \\ S \end{pmatrix} \quad (4.A.4)$$

We solve Eq. (4.A.4) by launching a traveling wave in the center of the device and calculating its reflection amplitude on one half of the device [63]. In order to find the envelope of the field, we discretize the device on a grid with spacing Λ. In this active mirror approach, the propagation over one lattice spacing is given by

$$\begin{pmatrix} R(x_i+\Lambda) \\ S(x_i+\Lambda) \end{pmatrix} \approx \quad \left(\boldsymbol{I} + \Lambda\tfrac{\partial}{\partial x}\right)\begin{pmatrix} R(x_i) \\ S(x_i) \end{pmatrix} \quad = \mathbf{M}_{x_i}\begin{pmatrix} R(x_i) \\ S(x_i) \end{pmatrix} \quad (4.A.5)$$

and the transfer matrix of one half of the device is:

$$\mathbf{M}_{\text{half}} = \quad \prod_{x_i=L/2}^{x_i=0}\mathbf{M}_{x_i} \quad = \begin{pmatrix} M_{00} & M_{01} \\ M_{10} & M_{11} \end{pmatrix} \quad (4.A.6)$$

where L is the length of the device. As there is no input from outside the device

$$\begin{pmatrix} R(x=\frac{L}{2}) \\ S(x=\frac{L}{2}) \end{pmatrix} = \begin{pmatrix} t \\ 0 \end{pmatrix} \mathbf{M}_{\text{half}} \Rightarrow \begin{pmatrix} R(x=0) \\ S(x=0) \end{pmatrix} = \mathbf{M}_{\text{half}} \begin{pmatrix} 1 \\ r \end{pmatrix} \tag{4.A.7}$$

where r is the reflection and t is the transmission of half of the device. At the laser threshold, the round trip through the device is stable, hence $|r| = \left|-\frac{M_{10}}{M_{11}}\right| = 1$. The sign of r gives the symmetry of the mode.

We search for the detuning $\delta\omega$ and gain $\alpha(x)$ for the threshold condition of the symmetric mode by minimizing $1-r$ with a Powell hybrid method. Both the refractive index change $\Delta n(x)$ and gain $\alpha(x)$ are taken to have a Gaussian profile with the size of the pump beam. The gain $\alpha(x) = \alpha_{\text{absorption}} + \alpha_{\text{pump}}(x)$ consists of a negative baseline, due to absorption in the unpumped areas, and is more positive in the pumped center. This amplitude of the gain due to pumping is varied to find the threshold condition. For the best fit we take $\Delta n(x)$ negative in the center of the pump beam and zero in the unpumped areas. A discussion about the exact amplitude of the index and gain profiles is included in the main text. Note that the radiated field is proportional to the asymmetric combination $R-S$, as discussed before.

The described transfer matrix method proved to be very powerful; it is not only useful to find the threshold conditions [88], but it can also be extended to calculate the mode spectrum below threshold, to provide insight in noise in the system [63, 89], and to study the occurence of spatial hole burning [90].

4.B Retrieval of the phase of light

Measuring the phase of light is a non-trivial task, because electronic detectors, such as photo diodes and CCDs, are to slow to operate at optical frequencies ($\sim 400\,\mathrm{THz}$). The phase of the light encodes the direction in which the light travels [91]. When both the phase and the intensity of monochromatic light are known, also its trajectory in the forward and backward directions are known. When propagating, the information in the phase and intensity mixes. This can be scrutinized to obtain the phase: after measuring the intensity at different distances, the phase information can be retrieved by Gerchberg-Saxton-like iterative algorithms [66].

Figure 4.4 schematically depicts a Gerchberg-Saxton-like iterative algorithm which we used to retrieve the phase information from intensity measurements at different distances [92, 93]. In our case, these locations are at an image plane of the near and the far-field of the sample. The propagation of the light between these two planes can be described by a Fourier transform. The phase is retrieved by numerically propagating between both planes and applying the measured information. This goes in successive steps: the measured intensity of the near field is combined with the best known near-field phase and propagated to the far field. Now, the intensity information is mixed with the phase, and a better phase estimation is obtained, while the propagated intensity contains less information. The propagated intensity is replaced by the measured intensity in the far field, and is propagated back to the near field plane. Again, the intensity and phase are mixed and a better phase

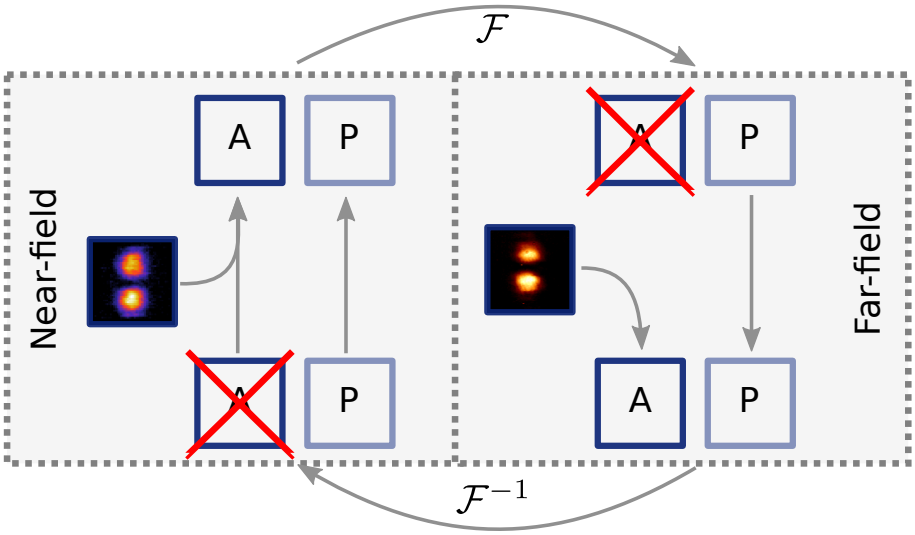

Figure 4.4: Schematic overview of iterative phase retrieval algorithm.

estimation is obtained. A good estimate of the phase is retrieved after several of such iterations [94].

This algorithm convergences after typically 50 iterations for our measurements. The first iteration is bootstrapped with a random phase pattern. In order to avoid local minima in this optimization procedure, the algorithm is run for 100 initial random phases and these results are averaged.

Faster and more reliable convergence can be obtained when more information about the sample is employed. In our case, we use the beam-block measurements to obtain a better first phase estimation as input for the final algorithm. This first phase estimation is obtained by running the algorithm with different intensity inputs in successive iterations. The near- and far-field measurements with the beam-block selecting in following places are used as inport: center, top, left, bottom, and right. This is sequence is repeated five times, and finalized with 10 iterations of the center measurements only. This reduces both the required number of iterations and increases the output stability.